Korean J. Chem. Eng., 37(11), 1975-1984 (2020)
DOI: 10.1007/s11814-020-0600-8

pISSN: 0256-1115
eISSN: 1975-7220

Fast and effective methylene blue adsorption onto graphene oxide/amberlite nanocomposite: Evaluation and comparison of optimization techniques

Zeynep Ciğeroğlu*,†, Gürkan Küçükyıldız, Aydın Haşimoğlu***, Fulya Taktak*, and Nazlıcan Açıksöz***

*Uşak University, Engineering Faculty, Department of Chemical Engineering, 64200 Uşak, Turkey
**Uşak University, Engineering Faculty, Department of Electrical and Electronics Engineering, 64200 Uşak, Turkey
***Gebze Technical University, Material Science and Engineering Department, Engineering Faculty, 41400 Gebze, Kocaeli, Turkey

(*Received 19 January 2020 • Revised 29 May 2020 • Accepted 3 June 2020*)

Abstract−Since graphene is a miracle material of the 21st century, a considerable number of researchers have studied the oxidation of graphite to synthesize graphene oxide and its applications. In this study, polymeric resin (amberlite XAD7HP) supported graphene oxide (GO) nanocomposite was synthesized successfully. Analytical methods, namely Fourier transform infrared spectroscopy (FTIR), X-ray diffraction (XRD), and scanning electron microscopy (SEM) were utilized to characterize the new structure. Methylene blue (MB) solution was selected as a model discharged textile wastewater for adsorption application of synthesized nanocomposite. The adsorption data were modelled by response surface methodology (RSM), random forest (RF) and artificial neural networks (ANN) methods. The optimal condition parameters, which maximize the adsorption uptake capability, were determined by the genetic algorithm. Statistical errors and correlation coefficient values of each developed model were calculated independently to compare models' performance. According to the results, the developed RF model outperformed the other models. On the other hand, the ANN model had the lowest correlation coefficient value among the models.

Keywords: Adsorption, Amberlite Resin, Graphene Oxide, Response Surface Methodology, Random Forest Model, Artificial Neural Network

INTRODUCTION

Environmental pollution is a common problem of all nations and threatens ecological life and living beings. One of the issues that cause this pollution is the dyes and pigments which are released uncontrolled to the environment. Dyes and pigments are used for many industries such as ink, plastic, fabric, cosmetics, food, leather, and textile. Especially, the textile industry uses about 1.3 million tons of pigments and dyes per year [1]. It is assumed that 280,000 tons of textiles dyes are discharged into the rivers, lakes and underground water resources per year [2]. Consequently, the life of the aquatic organisms is endangered. On the other hand, sunlight cannot pass through the polluted water, so photosynthesis is restricted [3]. Besides, eutrophication may occur due to dye effluents [4]. Many researchers have tried to cope with this problem and used different separation methods such as adsorption [5], photodegradation [6], electro-Fenton degradation [7], electro-coagulation [8], and biological treatments [9]. Among all, adsorption is the cheapest and the simplest method, so it is the most preferred one [10].

Methylene blue, which is generally used for coloring paper, dyeing wool and cotton [11,12], was selected as the model dye for our study. It is a basic and cationic dye which is known as low harmful material. Nevertheless, vomiting, eye burns, increased heart rate, diarrhea, gastritis, mental confusion, nausea symptoms could occur with too much acute exposure [13,14]. Furthermore, the value of oral lethal dose (LD_{50}) on rats and mice has been recorded as 1,180 and 3,500 $mgkg^{-1}$, respectively [15].

Graphene oxide (GO) has drawn great attention because of its two-dimensional (2D) honeycomb lattice, high transparency, and a large number of oxygenated groups [16]. GO and reduced graphene oxide (rGO) have been often preferred owing to the functional groups such as carboxylic acid and hydroxyl groups, which can easily bind with the functional groups of adsorbate [17]. Moreover, π-π interactions may have occurred between the aromatic groups of GO and the benzene ring of adsorbate [18]. In this study, amberlite resins were used as polymeric supporting material to conduct adsorption studies [19].

Response surface methodology (RSM), which is generally the preferred methodology for the optimization of adsorption experiments, includes both statistical data and mathematical models [20]. The number of experiments and energy demand could be minimized by using RSM [21].

Ghaedi et al. used the ANN algorithm to optimize parameters of phenol adsorption [22]. An ANN model, which has reported the minimum squared error (MSE) and the correlation coefficient (R^2) as 0.0022 and 0.972, respectively, was constructed for this purpose. The selected operation conditions were optimized by the constructed ANN model.

Cao et al. utilized the Fe_3O_4/rGO as an adsorbent material to remove the mercury from aqueous solutions [23]. The authors

†To whom correspondence should be addressed.
E-mail: zilbay@gmail.com, zeynep.ilbay@usak.edu.tr

modeled and optimized the gathered experimental data by using the ANN and GA, respectively. They compared the developed algorithm with the RSM and claimed that the developed optimization algorithm has higher correlation with the experimental data than RSM.

Cao et al. prepared a graphene oxide-supported nanoscale zero-valent iron (nZVI/rGO) composite to remove Se (IV) from aqueous solutions [24]. They developed an ANN model for the modeling of the experimental data and optimized parameters of the ANN for both the GA and PSO. They pointed out that the developed ANN-GA model outperformed for modeling and optimizing the experimental data.

Fan et al. synthesized nZVI/rGO magnetic nanocomposites to remove copper from aqueous solutions [25]. They utilized the ANN-GA and ANN-PSO algorithms for the modeling and prediction of experimental data. The adsorption temperature, initial pH, initial concentration of the copper solution and, adsorption time were optimized by the RSM, ANN-GA and ANN-PSO algorithms. It is observed from the results that the ANN-PSO model outperformed for the modeling and optimizing of the experimental data.

To the best of our knowledge, a novel polymeric resin (amberlite XAD-7HP) supported graphene oxide (GO) nanocomposite, which was not studied before, was prepared successfully for the removal of MB. The process optimization was carried out with the aid of RSM, GA, and ANN. Moreover, statistical error functions were applied to the experimental data. The morphology of the new composite adsorbent was analyzed by SEM, FTIR, and XRD techniques. Statistical parameters of each model were calculated to compare the developed methods' performance.

MATERIALS AND METHODS

1. Materials

Amberlite XAD-7HP resin, tetrahydrofuran (THF), sodium hydroxide, and hydrochloric acid were purchased from Sigma Aldrich. Graphene oxide nanosheets were purchased from Yasin Teknik Laboratory in İstanbul, Turkey.

2. Preparation of Polymeric Resin (Amberlite XAD7HP) Supported Graphene Oxide (GO) Nanocomposite

As an initial step, 10 mg of GO nanoplatelets was mixed with 50 mL of THF and sonicated in an ultrasonic bath for three hours to suspend graphene oxide in THF. Using the slightly modified preconditioning according to the procedure of Sun et al., the XAD-7HP resin was washed with 95% ethanol for three times [26]. After washing XAD-7HP resin, the amberlite resin was then added to the graphene oxide solution. The gathered mixture was agitated with a magnetic stirrer which operated at 400 rpm for one day. The solute was washed with ultrapure water (18.2 MΩ cm, Milli-Q water, Millipore) until pH was neutralized (pH~7).

3. Characterization of Polymeric Resin (Amberlite XAD7HP) Supported Graphene Oxide (GO) Nanocomposite

An FT-IR spectrometer (Agilent Cary 630) was operated to determine the characteristic functional groups of amberlite resin, GO nanosheet, and amberlite resin supported graphene oxide (GO) nanocomposite. The surface morphology of three materials was examined using a Quanta FEG-450 SEM. To characterize the crystal structure of the nanomaterials, X-ray Diffraction with Cu Kα radiation in the range of 5°-90° (2θ) measurements were conducted.

Table 1. Face-centered central composite design with coded levels

Independent variables	Coded levels		
	X_1 (−1)	X_2 (0)	X_3 (+1)
Initial concentration of MB (mgL^{-1})	10	55	100
Adsorbent dose (mg)	5	12.5	20
Adsorption time (min)	30	105	180

4. Face Centered-central Composite Design and Adsorption Experiments

RSM is a widely used statistical and mathematical technique for determining not only the synergic effects of independent parameters (inputs) but also the relationship between the dependent parameters (outputs) and inputs [27]. Furthermore, RSM provides the design of experiments through regression analysis and optimization [20]. Centered-composite design (CCD), which serves to estimate the quadratic polynomial response surface model, is one of the sample applications of RSM [28].

All experiments were conducted at pH 4 due to the results of the preliminary investigations. Three different variables, initial concentration of MB (10-100 mgL^{-1}), the amount of adsorbent (5-20 mg), and adsorption time (30-180 min), were selected to design experiments. Design-Expert software version 12-Stat-Ease (Trial version) program was used to construct face centered-central composite design (FCCCD). Center points were done at six times to evaluate the repeatability of experiments and decrease the data error. Therefore, the design was comprised of 20 experiments with six replicated central points. Table 1 indicates the FCCCD with coded value. In adsorption experiments, shaking speed was adjusted at 100 rpm, and the adsorption temperature was stabilized at 25 °C.

Adsorption uptake, the response of the system, can be calculated in Eq. (1) as follows:

$$q_{MB} = \frac{(C_i - C_e) \times V}{W} \quad (1)$$

where q_{MB} is the adsorption uptake of methylene blue onto amberlite/graphene oxide nanocomposite ($mg \cdot g^{-1}$), C_i and C_e are the initial concentration of MB and the equilibrium concentration of MB in aqueous solution as mg L^{-1}, respectively. V is the volume of solution as L and W is the mass of the adsorbent as g.

The Lambda 365 UV/Vis Spectrophotometer measured the initial and equilibrium concentrations of MB at 668 nm.

Generally, generating a second-order polynomial mathematical model represents association between factors and dependent variable. This model can be expressed in Eq. (2):

$$y = \beta_0 + \Sigma_{i=1}^{3} \beta_i x_i + \Sigma_{i=1}^{3} \Sigma_{j=1}^{3} \beta_{ij} x_i x_j + \Sigma_{i=1}^{3} \beta_{ii} x_i^2 \quad (2)$$

where y is the predicted adsorption uptake, x_i's are the selected variables (initial concentration of MB, amount of adsorbent, adsorption time). β_0 is the model constant, β_i is the linear coefficient, β_{ij} is the quadratic coefficient, β_{ij} is the cross-product coefficient.

Models and parameters could be statistically analyzed by the

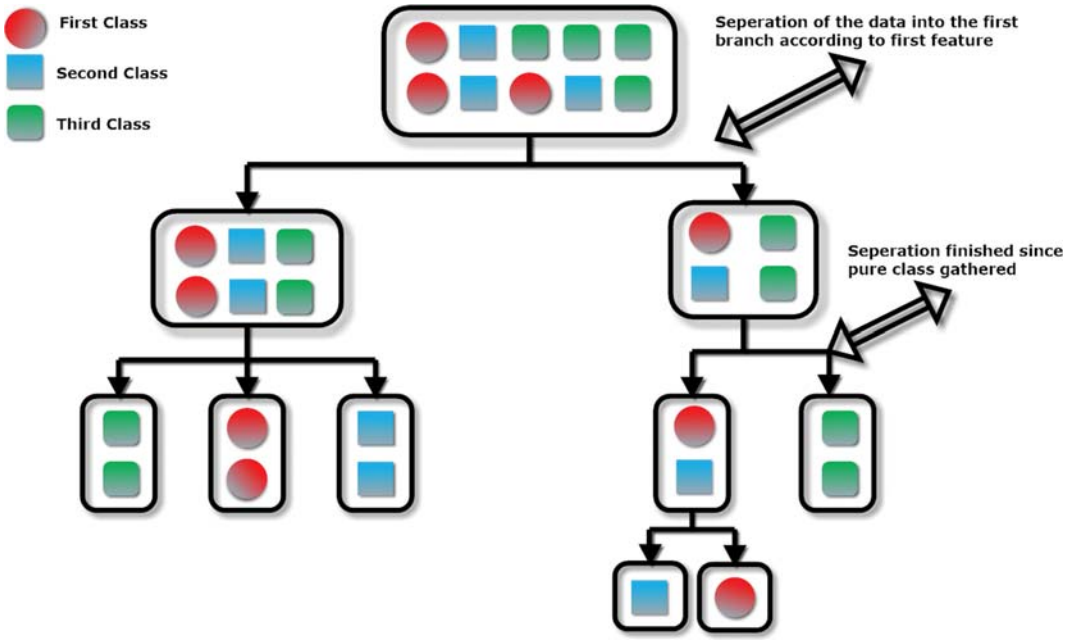

Fig. 1. Decision tree classification scheme.

ANOVA method embedded in the Design-Expert program. ANOVA test suggests the parameters most affecting the response by calculating F-test and p-value (probability) [29]. On the other hand, RSM also provides tridimensional graphs that depict the synergic effect of variables on the response.

5. Prediction by Random Forest

The decision tree algorithm was initially developed by Morgan and Sonquiest in 1963. After a study published by Breiman in 1984, the decision tree algorithm has become popular for researchers who study classification applications [30,31].

In the first step of the decision tree algorithm, the training data is separated into two groups based on a determined threshold according to the first feature (Fig. 1). The threshold value is determined by the minimization of the residual sum of squares given below in Eq. (3).

$$Rss = \Sigma(y_i - y_l)^2 + \Sigma(y_i - y_r)^2 \quad (3)$$

where y_i represents the value for the corresponding feature for the i-th sample. Similarly, y_l and y_r represent the mean values for samples, which are classified as the left and right nodes, respectively. In a binary decision tree, the separation process is applied to all nodes by using the next feature unless the pure class samples are obtained. Applying the separation process to all nodes can cause a mathematical payload since complex calculations are done for each step. Some nodes (features) can be more of a distinction between the classes. Therefore, useless nodes should be eliminated in order to reduce computational costs. The gini-index, which is given in Eq. (4), can be used to determine distinctive nodes.

$$Gini = N_l \sum_{k=1}^{Nl} p_{kl}(1 - p_{kl}) + N_r \sum_{k=1}^{Nr} p_{kr}(1 - p_{kr}) \quad (4)$$

where N_l and N_r represent the total number of samples, which are classified as the left and the right nodes, respectively. Similarly, p_{kl} and p_{kr} represent the proportions of kt-th class in the left and right nodes. The decision tree algorithm may not get satisfactory results in complex classification problems since the classification accuracy of the algorithm is highly dependent on the training data. Researchers have developed the forest structure, which consists of several decision trees, to overcome this problem. Therefore, in a random forest algorithm, trees are constructed from random subsets of the training data. The output of the random forest classifier, which is given in Eq. (5), can be calculated as the average outputs of the constructed trees.

$$RO = \frac{1}{N} \sum_{i=1}^{N} T_i \quad (5)$$

where N represents the total number of trees, and T_i represents the i-th tree's output.

In this study, the RF model was used to model the experimental data. The experimental data consisted of 20 samples. The dataset can be assumed as unbalanced due to its low sample size. Although the dataset was unbalanced, the RF algorithm could get satisfactory results. In the training phase of the RF model, randomly selected 15 samples (75%) of the dataset was used. The remaining five samples (25%) were used to evaluate the performance of the developed RF model. The tree number and min leaf size of the devel-

Table 2. Developed models' parameters

	Parameter name	Value
RF	Number of tree	100
	Min leaf size	5
ANN	Hidden layer size	2
	Neuron size	40
	Activation function	'Tansig'

oped RF Model were set as 100 and 5, respectively. These parameters were determined by trial and error model and given in Table 2.

6. Prediction by Artificial Neural Network (ANN)

ANN is a statistical machine learning technique which simulates some features of the human brain, such as learning, generalizing, or abstracting from experience. The ANN models can discern relationships between input and output. Therefore, ANNs can be easily applied to the complex problems which do not have algorithmic solutions. An ANN consists of interconnected nodes known as neurons. The output of a neuron can be calculated as follows in Eq. (6),

$$y_i = f((\Sigma_{i=1}^{N} x_i + w_i) + b) \quad (6)$$

where w is the weights, b is bias, and f is an activation function. The activation function could vary, such as hyperbolic tangent function, sigmoid function, threshold function relying on the problem. The training process of the model is modifying the weights and biases of neurons to diminish the error between the desired dependent variable and the output of the network. The training process continues until the error drops below a minimum value or the maximum number of training repetitions is reached. Once the network is trained, the neural network is then utilized to simulate system outputs for the unknown inputs. As in Fig. 2, the ANN consists of three parts: an input layer, a hidden layer(s), and an output layer. For a given modeling problem, the number of nodes in the input and output layers equals the numbers of input and output parameters. On the other hand, the number of nodes in the hidden layer(s) alters relying on the complicatedness of the problem.

In this study, in addition to the RF model, an ANN model was also used to model the experimental data. The model consisted of one input layer, two hidden layers, and one output layer. Each layer contained 3, 40, 40, 1 neuron, respectively. Similarly, to the RF model, 15 samples (75%) randomly selected of the dataset were used in the training phase of the ANN model. The remaining five samples (25%) were used to assess the performance of the developed ANN model. The number of hidden layers, neuron size per layer and activation function were determined as 2, 40 and 'tansig' respectively. The parameters are of the developed models were determined by trial and error model and given in Table 2.

7. Genetic Algorithm Optimization

The GA is used in various optimization problems thanks to its adaptable form. Contrary to conventional optimization techniques, the GA searches the entire solution space for the optimum solution without being trapped in local extremes. The GA escapes from the local extremes by the crossover and mutation operations. Therefore, the GA has a higher probability of finding the global extremum point in complex solution spaces [x-y] as compared to traditional methods.

In the GA, a generation, which comprises the populations, corresponds to an iteration of the algorithm. Initially, each member of the population is selected randomly, and a fitness value is calculated for each individual. Individuals correspond to possible solutions in a search space. An individual, also referred to as a chromosome, is composed of several genes. The evolution process is then performed on the individuals. The genes that have a better fitness score become dominant because of GA's genetic structure.

In this study, the GA was used to determine the optimal values of each input parameter in a predetermined range. Each distinct parameter is represented by a gene in the chromosome sequence of an individual. The value of a gene corresponds to the value of the input parameter. The fitness score of an individual depends on its gene sequence and is evaluated based on a pre-determined fitness function. At each iteration, the GA selects two individuals hav-

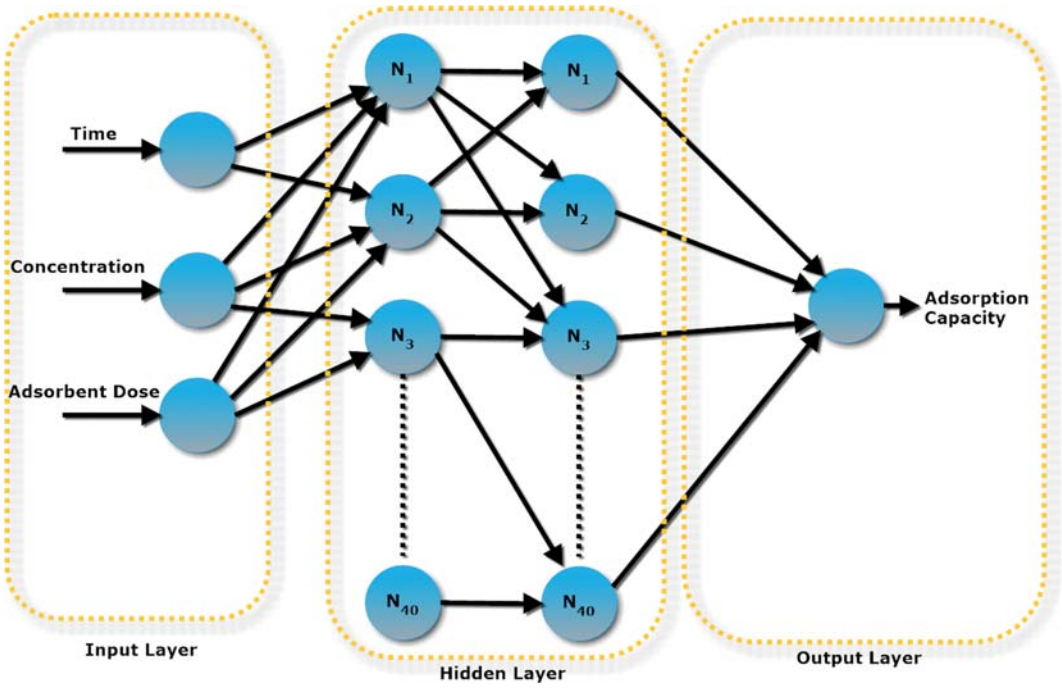

Fig. 2. The developed ANN model.

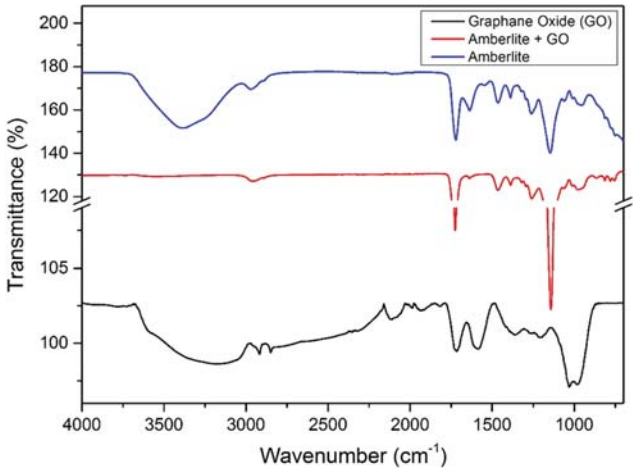

Fig. 3. FTIR spectrum of GO, amberlite XAD-7HP and polymeric resin (amberlite XAD-7HP) supported graphene oxide (GO) nanocomposite.

ing the highest fitness scores and places them in a mating pool. New individuals and children are produced owing to the crossover and mutation operations. The evolutionary cycle continues until a termination condition is met.

RESULTS AND DISCUSSION

1. Characterization Results of Adsorbent

FT-IR spectrum of amberlite (XAD-7HP), graphene oxide (GO), and GO-amberlite composite is shown in Fig. 3. In the spectrum of amberlite, a broad and strong band centered at 3,390 cm^{-1} was assigned to the absorbed water molecules in the polymeric network of amberlite. The small peak at 2,971 cm^{-1} and its shoulder on the right are attributed to the stretching mode of aliphatic C-H groups. On the other hand, the sharp absorption peaks at 1,465 cm^{-1} and 1,390 cm^{-1} arose from C-H deformations of CH_3. The strong and sharp peak at 1,721 cm^{-1} corresponded to C=O stretching. The band at 1,250 cm^{-1} was due to the vibrations of the C-C and C-O bonds. The peak at 1,147 cm^{-1} originated from the vibrations of ester oxygen and the following two carbons bonded to it in the polymeric chain.

The strong band located about 3,200 cm^{-1} originated from stretching modes of hydroxyl groups which were bonded to graphene layers. The diffuse and intense band was formed with shoulders. This band could be the result of hydroxide groups having different chemical environment on the carbon skeleton. As a result, -OH groups vibrated with different frequencies and resulted in a diffuse band. Moreover, water molecules in the graphene structure were another reason for intense and wideband formation in the spectra. The sharp peaks at about 1,700 cm^{-1} and 1,600 cm^{-1} were the result of stretching vibrations of carbonyl (C=O) groups and aromatic carbon-carbon double bond (-C=C-) vibrations in the graphene structure, respectively. The last two strong peaks at 1,232 cm^{-1}, 1,050 cm^{-1}, and the shoulder at 1,377 cm^{-1} were related to epoxy (C-O-C), alkoxy (C-OH) and carbonyl (O-C=O) groups, respectively. It was clear that graphene oxide was synthesized suc-

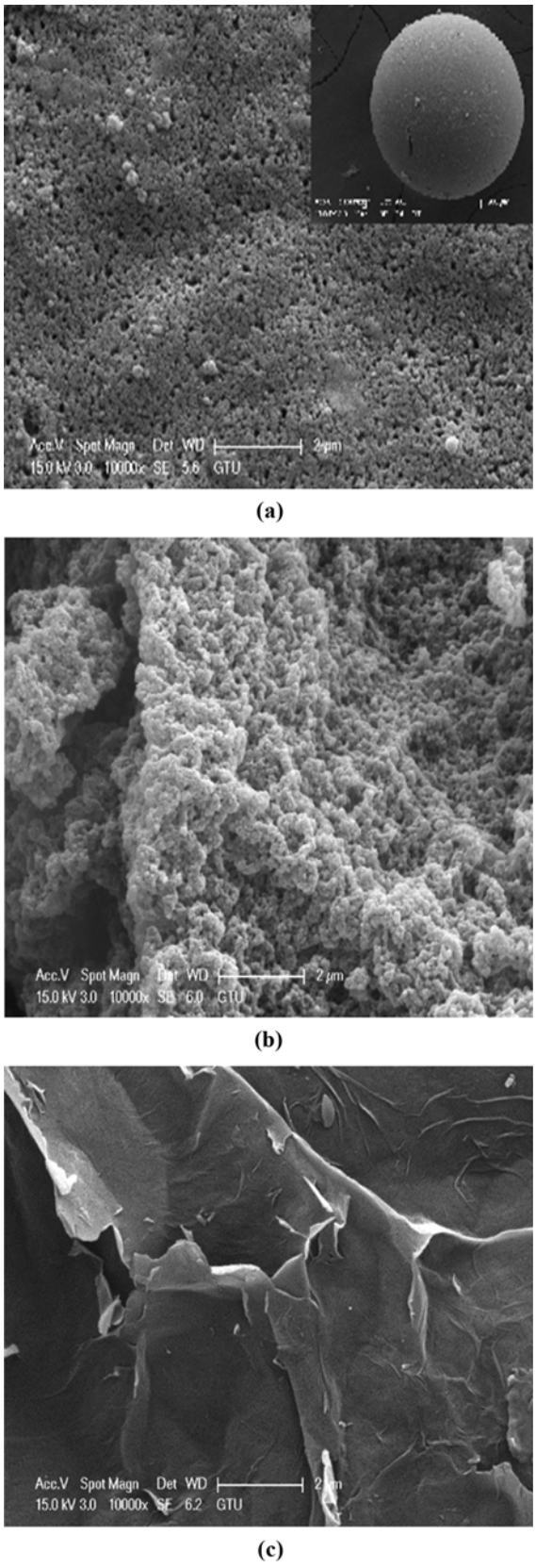

Fig. 4. SEM microphotograph of (a) pure amberlite, (b) polymeric resin (amberlite XAD-7HP) supported graphene oxide (GO) nanocomposite, (c) pure graphene oxide at magnification x10000, scale bar: 1 μm.

cessfully using a modified Hummer's method.

Up to now, amberlite and GO structure were investigated using the FT-IR technique. Amberlite-GO composite is also shown in the middle of Fig. 3. The spectrum of amberlite-GO composite was not so different from the one of amberlite. The primary difference was the disappearance of the wide hydroxyl band which was located at 3,390 cm^{-1}. This indicates that the drying of the composite was successful. In fact, there was still a very weak diffuse peak at about 3,300 cm^{-1} which may be the result of a small amount of GO doping.

As seen in the micrograph at high magnification in Fig. 4(a), pure amberlite XAD-7HP resin possessed spherical particulate morphology. Uniformly packed resin spheres produced superficial pores and a flat surface. After introduction of GO to resin, the surface of the microstructure underwent a transition from smooth to rough due to the agglomeration of spheres on the large GO sheets as shown in Fig. 4(c).

To evaluate the structural changes after the formation of GO, amberlite and GO/amberlite composite were characterized by X-ray diffraction analysis (XRD) and are shown in Fig. 5. The characteristic crystalline structure of GO proved by a sharp peak of GO at 2θ=11.54 (corresponding to a d-spacing value of 0.766 nm). Observation of a single peak having great intensity in the XRD pattern of GO shows that graphite is sufficiently oxidized during conversion to GO used in the study.

On the other hand, GO peak at 2θ=11.54 was dramatically flattened and slightly shifted (2θ=12.96) in the X-ray pattern of GO/amberlite composite. The diminishing of the crystallinity of GO represents the good dispersion of GO in the produced GO/amberlite. Besides, it is explained by the amorphous structure of amberlite, which became predominant due to insertion among the stacked layers of GO. Also, the amorphous structure of amberlite is confirmed by the absence of any characteristic peak in the x-ray pattern.

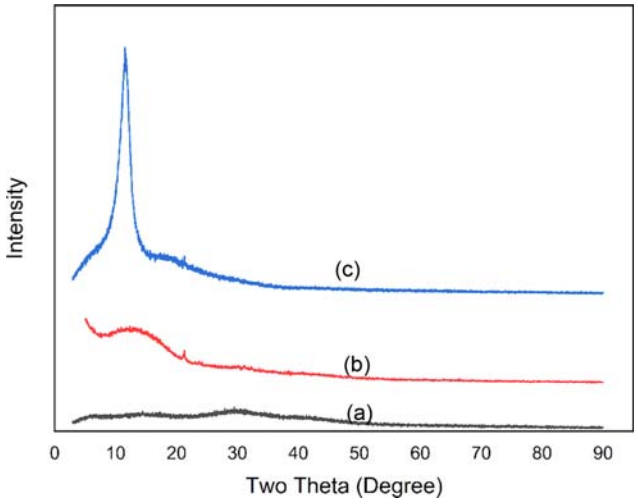

Fig. 5. X-ray diffraction analysis of (a) pure amberlite, (b) polymeric resin (amberlite XAD-7HP) supported graphene oxide (GO) nanocomposite, (c) pure GO.

2. Statistical Analysis and 3-D Graphs via RSM

Table 3 points out the ANOVA results consisting of F-value and p-value (probability) of generated models and factors. Traditionally, a high F-value and a p-value less than 0.05 are desired. ANOVA table depicts that the model was seen to be significant due to the F-value of 125.40 and p-value of <0.0001. It is observed from the results that the initial concentration, which has the highest F-value (580.77) and the lowest p-value (<0.0001), was the most crucial factor among the factors. Factors affecting adsorption uptake could be arranged in the following order: Initial concentration of MB> adsorbent dose>binary interactions of these variables>square of adsorbent dose.

Fig. 6(a)-(c) represents the 3-D graphs which belong to binary interactions of adsorbent dose-initial concentration of MB, the time-initial concentration of MB, time-adsorbent dose on the response, respectively.

Adsorption dose is an influential parameter on the adsorption process since it determines the adsorbent capacity at a given specified concentration. Higher adsorbent dose leads to the lower adsorption capacity due to the split in the concentraction gradient which occured between the solute and adsorbed solute [32]. There

Table 3. ANOVA Table for the adsorption uptake of MB onto polymeric resin (amberlite XAD-7HP) supported graphene oxide (GO) nanocomposite

Source	Sum of squares	df	Mean square	F-value	p-Value	
Model	33402.48	9	3711.39	125.40	<0.0001	Significant
A-Initial concentration of MB	17189.28	1	17189.28	580.77	<0.0001	
B-Adsorbent dose	9888.97	1	9888.97	334.12	<0.0001	
C-Adsorption time	4.61	1	4.61	0.1558	0.7014	
AB	4902.07	1	4902.07	165.63	<0.0001	
AC	3.32	1	3.32	0.1123	0.7444	
BC	3.48	1	3.48	0.1175	0.7389	
A^2	5.29	1	5.29	0.1789	0.6813	
B^2	905.41	1	905.41	30.59	0.0003	
B^2	2.66	1	2.66	0.0898	0.7706	
Residual	295.97	1	29.60			
Pure error	3.51	5	0.7023			
Cor total	33698.45	9				

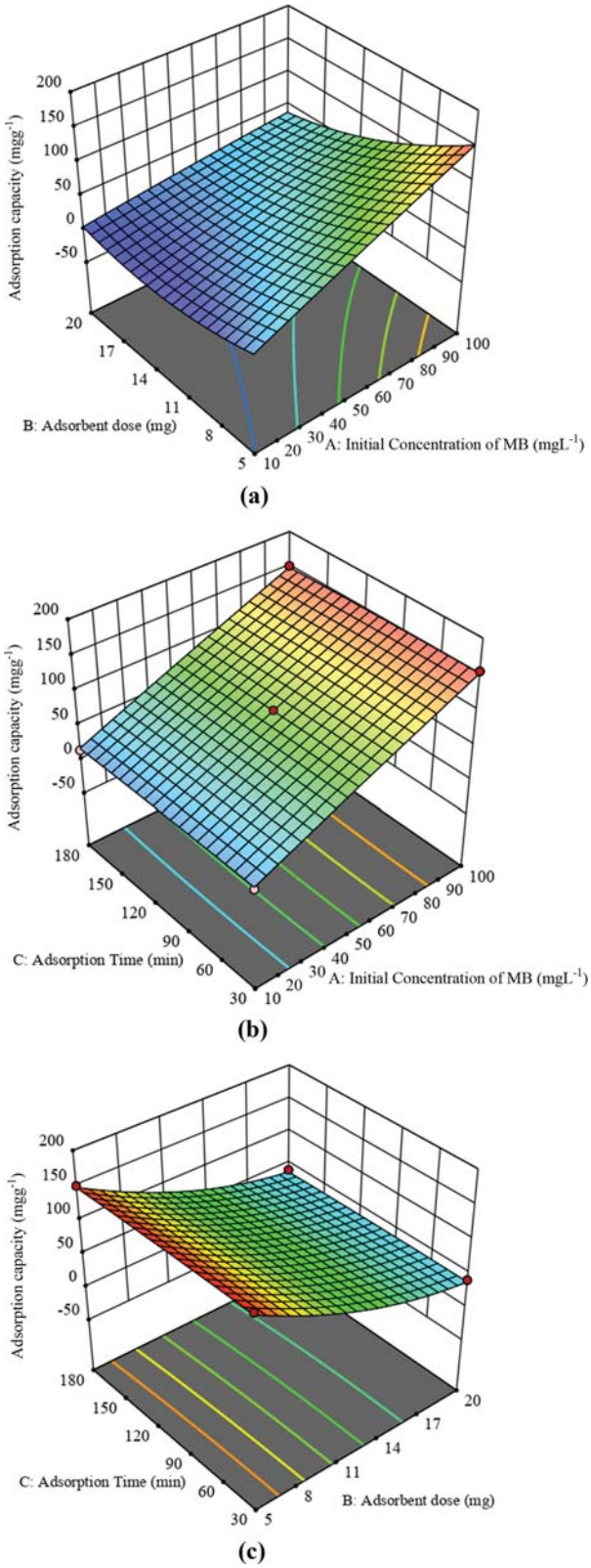

Fig. 6. (a) binary interaction of adsorbent dose and initial concentration of MB on response (Time=52.46 min), (b) binary interaction of time and initial concentration of MB on response (adsorption dose=5 g), (c) binary interaction of time and adsorbent dose on response (initial concentration of MB=100 mgL^{-1}).

is an inverse relationship between the adsorbent dose and qe, as can be seen in Eq. (1). The obtained results were consistent with similar studies in the literature [33,34].

At the same time, the increase in the viscosity of suspension hinders the diffusion of dye onto the adsorbent surface, according to the Stokes-Einstein equation. Fig. 6(a) and 6(c) confirmed the aforementioned phenomenon.

Higher initial concentration contributes to higher adsorption uptake; this result could be attributed to Fick's first law. According to Fick's law, flux is in direct proportion to the concentration gradient. Namely, a high concentration gradient is the driving force for diffusion of dye molecules onto the surface of the adsorbent [35]. Briefly, our adsorption results are confirmed in this phenomenon in Fig. 6(a) and 6(b).

The time should be considered as an essential factor for the adsorption process owing to economic reasons. The conducted experimental results proved that adsorption uptake increased with increasing time in our experimental range. That is, the adsorbent has a large number of vacant surface sites, and so the repulsive force interactions between the dye molecules on adsorbent and bulk phase occur easily [36]. It was figured out from Fig. 6(b) and 6(c) that the adsorption process was not at equilibrium because the adsorption uptake was still increasing.

3. Evaluation of Calculated Errors of RSM, RF, and ANN

The mathematical model equation in terms of actual factors through RSM is given in Eq. (7).

$$q_{MB}=+36.44+1.93A-8.34B+0.024C-0.073AB-0.00019AC+0.00117AC-0.000685A^2+0.322578B^2-0.000175C^2 \quad (7)$$

According to this equation, the predicted RSM model was calculated.

As mentioned previously, the RF and ANN models were developed to model the experimental data. The performance of the proposed RSM, RF, and ANN models was evaluated based on statistical parameters mean square error, root mean square error, mean absolute error, mean absolute percentage error. The parameters are defined by (Eq. (8)-(11)),

$$MSE=\frac{1}{n}\Sigma_{t=1}^{N}e_t^2 \quad (8)$$

$$RMSE=\sqrt{\frac{1}{n}\Sigma_{t=1}^{N}e_t^2} \quad (9)$$

$$MAE=\frac{1}{n}\Sigma_{t=1}^{N}|e_t| \quad (10)$$

$$MAPE=\frac{100\%}{n}\Sigma_{t=1}^{N}\left|\frac{e_t}{y_t}\right| \quad (11)$$

where e_t is the error and y_t is the output.

The determination of coefficient (R^2), which depicts the strength of the relationship between two variables, is an essential parameter for the models. The correlation coefficient is defined by (Eq. (12)),

$$r=\frac{n\left(\sum_{n=1}^{N}x_n\right)-(\Sigma_{n=1}^{N}x_n)(\Sigma_{n=1}^{N}y_n)}{\sqrt{\left[n\sum_{n=1}^{N}x_n^2-\left(\sum_{n=1}^{N}x_n\right)^2\right]\left[n\sum_{n=1}^{N}y_n^2-\left(\sum_{n=1}^{N}y_n\right)^2\right]}} \quad (12)$$

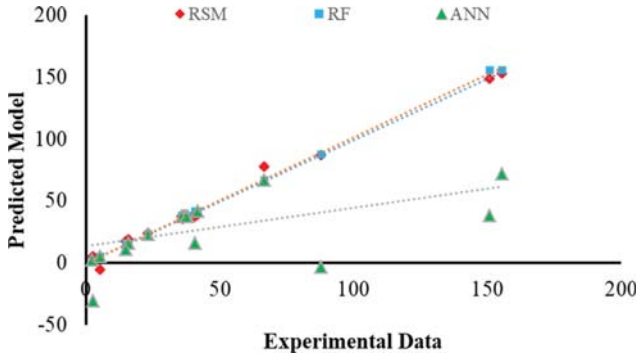

Fig. 7. Predicted model data for RSM, ANN and RF vs. Experimental data.

Table 4. Investigation of the performance results of RSM, RF and ANN models

Parameter	RSM model value	RF model value	ANN model value
R	0.9960	0.9995	0.6013
R^2	0.9921	0.9990	0.3615
MSE	14.81	1.89	1.48×10^{-3}
RMSE	3.85	1.37	38.57
MAPE	24.27	2.43	79.41
MAE	2.48	0.75	17.79

where N is the sample size of variables.

Fig. 7 depicts the generated models via RSM, RF, and ANN versus experimental data. In this study, the model that approaches the experimental data is the artificial neural network. The determination coefficient (R^2) shows the compatibility of experimental data and model data. Among the three applied models, the model with the highest coefficient of determination (0.9993) belongs to the artificial neural networks.

Table 4 indicates the experimental errors statistically with various error functions, such as mean square error, root mean square error. Assessing systematic errors, these errors should be quite small. The RF model obtained the highest determination coefficient (0.990). The RF model had the best correlation coefficient value (0.9995). The ANN model obtained the lowest determination coefficient. Thus, both ANN and RSM models showed a good correlation between actual values and modelled values. The applied ANN model indicated the lowest statistical errors. This means that the RF model predicts the best experimental data. When statistical error values, determination coefficients and also correlation coefficient (R) values were evaluated, it was understood that the neural network data is not well fit with experimental data.

4. Optimization of Parameters by GA

In this study, the GA was used to determine the optimal values of each input parameter in a predetermined range. Each distinct parameter is represented by a gene in the chromosome sequence of an individual. The value of a gene corresponds to the value of the input parameter. The fitness score of an individual depends on its gene sequence and is evaluated based on a predetermined fitness function. At each iteration, the GA selects two individuals having the highest fitness scores and places them in a mating pool.

Table 5. Determined optimal values

Models	Initial concentration of MB	Adsorbent dose	Adsorption time	Response
RF+GA	87.03	7.43	56.68	155.25
ANN+GA	77.28	8.27	53.37	154.72
RSM	100	5	52.456	152.67

The new individuals and the children are produced owing to the crossover and mutation operations. The evolutionary cycle continues until a termination condition is met.

The optimal values of each method are given in Table 5. The optimal conditions of RSM were found to be 100 mgL^{-1} as the initial concentration of MB, 5 mg as adsorbent dose and 52.46 min as adsorption time. In contrast, RSM predicted the optimal values as 7.43 mg of adsorbent dose, 87.03 mgL^{-1} of the initial concentration of MB, 56.68 min of adsorption time. On the other hand, ANN-GA suggested optimal conditions as 77.28 mgL^{-1} initial concentration of MB, 8.27 mg of adsorbent dose, 53.37 min of adsorption time. The optimized adsorption uptake values were found to be 155.25, 154.72, and 152.67 for RF+GA, ANN+GA, and RSM, respectively. The optimal values were determined differently depending on the methods since the genetic algorithm is a heuristic optimization technique. Therefore, the GA could determine different results at each algorithm cycle for the same optimization problem. Similarly, in this study, the genetic algorithm was performed 100 times and the determined results were averaged. On the other hand, the R^2 value of each model is unique. RSM uses a numerical optimization method by applying the desirability function.

Fig. 7 shows the data of developed models (RSM, ANN, and RF) versus experimental data. From Fig. 7, it can be said that predicted data were estimated more accurately by RF+GA than two other models. However, predicted data of RSM were good agreement in experimental data, according to ANN+GA.

Table 6 demonstrates the several optimization studies for MB uptake onto numerous adsorbents in the literature. From this table, it can be concluded that the synthesis of polymeric resin (amberlite XAD-7HP) supported graphene oxide (GO) nanocomposite was successfully achieved. Besides, it showed as a potential adsorbent for MB uptake from aqueous solution when compared with other several adsorbents in the literature.

CONCLUSIONS

Amberlite XAD-7HP resin supported graphene oxide (GO) nanocomposite was prepared and used for an adsorbent material to remove MB from aqueous solutions. Three experimental factors, namely the initial concentration of MB, adsorbent dose and adsorption time were selected as input data, while adsorption uptake of MB was considered as output. Twenty experiments with six replicates of central points were conducted according to face-centered central composite design. Experimental data were modeled by RSM, RF, and ANN. 3D graphs showed that the initial concentration of MB was the crucial factor in response. ANOVA table indicated the effectiveness of parameters on response with F-value and p-value.

Table 6. Comparison of adsorbent uptake of polymeric resin (amberlite XAD-7HP) supported graphene oxide (GO) nanocomposite with numerous adsorbents reported in the literature

Adsorbent	Adsorption capacity (mg/g)	Ref.
Hydrogel composite	1336.05	Liu et al. [37]
waste tea activated carbon	554.30	Auta et al. [38]
kapok fiber treated by sodium chlorite	110.13	Liu et al. [39]
Zeolite NaA	64.8	Sapawe et al. [40]
Activated carbon from dross licorice	82.90	Ghaedi et al. [41]
Albizia lebbeck seed pods	381.22	Ahmed et al. [42]
Spent coal based activated carbon	370.37	Xin-hui et al. [43]
Spent catalyst from vinyl acetatesynthesis as porous carbon	436.00	Duan et al. [44]
$ZnCl_2$-activated carbon from macadamia nut endocarp	194.70	Junior et al. [45]
Ruthenium nanoparticle-loaded activated carbon	41.64	Mazaheri et al. [46]
ZnS : Cu nanoparticle loaded on activated carbon	106.9	Asfaram et al. [47]
Oil palm leaves	103.02	Setiabudi et al. [48]
Chemically modified agriculture by-product	78.74	Azzaz et al. [49]
India shrub wood	257.73	Pirsaheba et al. [50]
Metal Organic Framework MIL-68(Al)	1666.67	Tehrani et al. [51]
Karanj fruit hulls	239.40	Islam et al. [52]
Anaerobic co-digestion of Agri-food organic waste	285.71	Anfar et al. [53]
Zn(OH)2-NPs—AC from cherry tree, activated carbon from cherry tree	41.49, 19.46	Ardekani et al. [54]
Graphene-like carbon	20.00	Lingamdinne et al. [55]
Catecholamine/Starch Superadsorbent	2276.50	Mahmoodi-Babolan et al. [56]
Ho-CaWO4	103.09	Igwegbe et al. [57]
Eggshell-treated palm oil fuel ash	714.29	Hasan et al. [58]
Zr-SBA-15	310.88	Ramezani et al. [59]
Amberlite resin supported GO	155.25	This study

Statistical parameters were computed to determine the error between the experimental data and models' output. According to the results, the RF model had a higher correlation coefficient with the actual data. On the other hand, the RSM model had 0.9960 correlation coefficient, which is satisfactory for the experimental data modeling.

REFERENCES

1. M. Yusuf, *Handbook of renewable materials for coloration and finishing*, Wiley-VCH, Weinheim (2018).
2. H. Ali, *Water, Air, Soil Pollut.*, **213**, 251 (2010).
3. T. L. Hu and S. C. Wu, *Bioresour. Technol.*, **77**(1), 93 (2001).
4. K. G. Bhattacharyya and A. Sharma, *Dyes Pigm.*, **65**, 51 (2005).
5. C. Sabarinathan, P. Karuppasamy, C. T. Vijayakumar and T. Arumuganathan, *Microchem. J.*, **146**, 315 (2019).
6. M. Saeed, M. Muneer, N. Akram, A. ul Haq, N. Hafzal and M. Hamayun, *Chem. Eng. Res. Des.*, **148**, 218 (2019).
7. G. Xia, Y. Lu, X. Gao, C. Gao and H. Xu, *Clean Soil Air Water.*, **43**, 229 (2015).
8. A. K. Golder, A. N. Samata and S. Ray, *J. Hazard. Mater.*, **127**, 140 (2005).
9. F. Afshariani and A. Roosta, *J. Cleaner Prod.*, **225**, 133 (2019).
10. M. Ghaedi, K. Mortazavi, K. Jamshidi, M. Roosta and B. Karami, *Toxicol. Environ. Chem.*, **94**, 846 (2012).
11. M. Ertaş, B. Acemoğlu, M. H. Alma and M. Usta, *J. Hazard. Mater.*, **183**, 421 (2010).
12. S. C. Nunez, T. M. Yoshimura, M. S. Ribeiro, H. C. Junqueria, C. Maciel, M. D. Countinhoneto and M. S. Baptista, *J. Photochem. Photobiol. B.*, **150**, 31 (2015).
13. M. M. Abd EI-Latif, A. M. Ibrahim and M. F. EI-Kady, *J Am Sci.*, **6**(6), 267 (2010).
14. D. Ghosh and K. G. Bhattacharyya, *Appl. Clay Sci.*, **20**, 295 (2002).
15. R. J. Lewis, *Sax's dangerous properties of industrial materials*, 11th Ed. Wiley-Interscience Publication, Wiley & Hoboken, New Jersey (2004).
16. N. R. Wilson, P. A. Pandey, R. Bealand, R. J. Young, I. A. Kinloch, L. Gong and J. Sloan, *ACS Nano.*, **3**, 2547 (2009).
17. H. L. Ma, Y. Zhang, Q. H. Hu, D. Yan, Z. Z. Yu and M. Zhai, *J. Mater. Chem.*, **22**, 5914 (2012).
18. A. Dabrowski, P. Podkoscienly, Z. Hubicki and M. Barzak, *Chemosphere*, **58**(8), 1049 (2005).
19. A. Islam, M. A. Laskar and A. Ahmad, *Environ. Monit. Assess.*, **175**, 201 (2011).
20. R. H. Myers, D. C. Montgomery and C. M. Anderson-Cook, *Response surface methodology: process and product optimization using designed experiments*, John Wiley & Sons, USA (2016).
21. C. Camposeco-Negrete, *J. Cleaner Prod.*, **91**, 109 (2015).
22. M. Ghaedi, A. Daneshfar, A. Ahmadi and M. S. Momeni, *J. Ind. Eng. Chem.*, **21**, 587 (2015).

23. R. Cao, M. Fan, J. Hu, W. Ruan, K. Xiong and X. Wei, *Materials*, **10**, 1279 (2017).
24. R. Cao, M. Fan, J. Hu, W. Ruan, X. Wu and X. Wei, *Materials*, **11**, 428 (2018).
25. M. Fan, J. Hu, R. Cao, K. Xiong and X. Wei, *Sci. Rep.*, **7**, 18040 (2017).
26. L. Sun, Y. Guo, C. Fu, J. Li and Z. Li, *Food Chem.*, **136**, 1022 (2013).
27. D. C. Montgomery, *Design and analysis of experiments*, John Wiley & Sons, New York (2017).
28. G. E. Box and N. R. Draper, *Empirical model-building and response surfaces*, John Wiley & Sons, New York (1987).
29. G. Box, W. C. Hunter and J. C. Stuart, *Statistics for experimenters. An introduction to desing, data analysis, and model building*, Wiley, New York (1978).
30. J. N. Morgan and R. C. Messenger, *THAID a sequential analysis program for the analysis of nominal scale dependent variables*, Ann Arbor, Survey Research Center, Institute for Social Research, University of Michigan (1973).
31. L. Breiman, J. Friedman, C. J. Stone and R. A. Olshen, *Classification and regression trees*, CRC Press, New York (1984).
32. P. S. Kumar, S. Ramalingam and K. Sathishkumar, *Korean J. Chem. Eng.*, **28**(1), 149 (2011).
33. X. Han, X. Niu and X. Ma, *Korean J. Chem Eng.*, **29**(4), 494 (2012).
34. T. Liu, Y. Li, Q. Du, J. Sun, Y. Jiao, G. Yang, Z. Wang, Y. Xia, W. Zhang, K. Wang, H. Zhu and D. Wu, *Colloid Surf. B.*, **90**, 197 (2012).
35. F. C. Wu, R. L. Tseng and R. S. Juang, *Water Res.*, **35**, 613 (2001).
36. C. H. Wu, *J. Hazard. Mater.*, **144**, 93 (2007).
37. Y. Liu, Y. Zheng and A. Wang, *Adsorpt. Sci. Technol.*, **28**, 913 (2010).
38. M. Auta and B. H. Hameed, *Chem. Eng. J.*, **175**, 233 (2011).
39. Y. Liu, J. Wang, Y. Zheng and A. Wang, *Chem. Eng. J.*, **184**, 248 (2012).
40. N. Sapawe, A. A. Jalil, S. Triwahyono, M. I. A. Shah, R. Jusoh, N. F. M. Salleh, B. H. Hameed and A. H. Karim, *Chem. Eng. J.*, **229**, 388 (2013).
41. M. Ghaedi, M. D. Ghazanfarkhani, S. Khodadoust, N. Sohrabi and M. Oftade, *J. Ind. Eng. Chem.*, **20**, 2548 (2014).
42. M. J. Ahmed and S. K. Theydan, *J. Anal. Appl. Pyrolysis.*, **105**, 199 (2014).
43. D. Xin-hui, C. Srinivasakannan and L. Jin-sheng, *J. Taiwan Inst. Chem. E*, **45**, 1618 (2014).
44. X. Duan, Z. Zhang, C. Srinivasakannan, F. Wang and J. Liang, *Chem. Eng. Res. Des.*, **92**, 1249 (2014).
45. O. P. Junior, A. L. Cazetta, R. C. Gomes, É. O. Barizão, I. P. A. F. Souza, A. C. Martins, T. Asefa and V. C. Almeida, *J. Anal. Appl. Pyrolysis.*, **105**, 166 (2014).
46. H. Mazaheri, M. Ghaedi, S. Hajati, K. Dashtiana and M. K. Purkaitc, *RSC Adv.*, **5**, 83427 (2015).
47. A. Asfaram, M. Ghaedi, S. Hajati, M. Rezaeinejad, A. Goudarzi and M. K. Purkait, *J. Taiwan Inst. Chem. E*, **53**, 80 (2015).
48. H. D. Setiabudi, R. Jusoh, S. F. R. M. Suhaimi and S. F. Masrur, *J. Taiwan Inst. Chem. E.*, **63**, 363 (2016).
49. A. A. Azzaz, S. Jellali and L. Bousselmi, *Optimization of a cationic dye adsorption onto a chemically modified agriculture by-product using response surface methodology*, 7th International Renewable Energy Congress (IREC), Hammamet, 1-5 (2016).
50. M. Pirsaheb, Z. Rezai, A. M. Mansouri, A. Rastegar, A. Alahabadi, A. R. Sani and K. Sharafi, *Desalin. Water Treat.*, **57**, 5888 (2016).
51. M. S. Tehrani and R. Zare-Dorabei, *RSC Adv.*, **6**, 27416 (2016).
52. M. A. Islam, S. Sabar, A. Benhouria, W. A. Khanday, M. Asif and B. H. Hameed, *J. Taiwan Inst. Chem. E*, **74**, 96 (2017).
53. Z. Anfar, R. El Haouti, S. Lhanafi, M. Benafqir, Y. Azougarh and N. El Alem, *J. Environ. Chem. Eng.*, **5**, 5857 (2017).
54. P. S. Ardekani, H. Karimi, M. Ghaedi, A. Asfaram and M. K. Purkait, *J. Mol. Liq.*, **229**, 114 (2017).
55. L. P. Lingamdinne, J. Singh, J. S. Choi, Y. Y. Chang, J. K. Yang, R. R. Karri and J. R. Koduru, *J. Mol. Liq.*, **265**, 416 (2018).
56. N. Mahmoodi-Babolan, A. Heydari and A. Nematollahzadeh, *Bioresour. Technol.*, **294**, 122084 (2019).
57. C. A. Igwegbe, L. Mohmmadi, S. Ahmadi, A. Rahdar, D. Khadkhodaiy, R. Dehghani and S. Rahdar, *MethodsX*, **6**, 1779 (2019).
58. R. Hasan, C. C. Chong, H. D. Setiabudi, R. Jusoh and A. A. Jalil, *Environ. Technol. Innovation*, **13**, 62 (2019).
59. F. Ramezani and R. Zare-Dorabei, *Polyhedron*, **166**, 153 (2019).